PERFORMANCE CHARACTERIZATION OF A LANDMARK MEASUREMENT SYSTEM FOR ARRM TERRAIN RELATIVE NAVIGATION

Michael A. Shoemaker[*]**, Cinnamon Wright**[†]**, Andrew J. Liounis**[‡]**, Kenneth M. Getzandanner**[†]**, John M. Van Eepoel**[§]**, and Keith D. DeWeese**[§]

This paper describes the landmark measurement system being developed for terrain relative navigation on NASA's Asteroid Redirect Robotic Mission (ARRM), and the results of a performance characterization study given realistic navigational and model errors. The system is called Retina, and is derived from the stereophotoclinometry methods widely used on other small-body missions. The system is simulated using synthetic imagery of the asteroid surface and discussion is given on various algorithmic design choices. Unlike other missions, ARRM's Retina is the first planned autonomous use of these methods during the close-proximity and descent phase of the mission.

INTRODUCTION

NASA's Asteroid Redirect Robotic Mission (ARRM) is the robotic mission to visit an asteroid and retrieve a boulder from its surface as a precursor to the manned Asteroid Retrieval Mission (ARM).[1,2] The target launch date for ARRM is in January 2021, and the current asteroid target is 2008 EV5. After the spacecraft begins operations in the vicinity of the asteroid, the characterization phase will refine the shape, spin, and gravity models as well as obtain high resolution imagery of the surface. Two descent and boulder collection dry runs will be performed prior to the actual descent to the surface of the asteroid. After the boulder is captured the spacecraft will perform an ascent maneuver, drift to a safe distance away, then insert into a halo orbit along the vbar of the asteroid for a period of time to perform a gravity tractor demonstration before returning the boulder to cislunar space for later exploration by the ARM crewed mission.

Both optical navigation and terrain-relative navigation (TRN) are important components in the guidance, navigation, and control (GN&C) while the vehicle is near the asteroid. One of the most critical phases of the mission is the descent from 50 m altitude to the surface of the asteroid. As the vehicle descends closer to the surface, autonomous TRN is required to maintain the descent trajectory to the target boulder. The spacecraft must be centered over the boulder with dispersions of less than 50 cm (3-σ). Moreover, the navigation must be autonomous because of the communication

[*]Senior Systems Engineer, a.i. solutions, Inc., 4500 Forbes Blvd., Lanham, MD, 20706.

[†]Aerospace Engineer, Navigation and Mission Design Branch (Code 595), NASA Goddard Spaceflight Center, Greenbelt, MD 20771, USA.

[‡]Pathways Intern, Navigation and Mission Design Branch (Code 595), NASA Goddard Spaceflight Center, Greenbelt, MD 20771, USA.

[§]Aerospace Engineer, Attitude Control Systems Engineering Branch, NASA Goddard Spaceflight Center, Greenbelt, MD 20771, USA.

light-time delays. This autonomous TRN is partially achieved with a system to match observed landmarks with onboard terrain maps. Retina is a tool being developed at NASA Goddard Space Flight Center to make line-of-sight (LOS) measurements to predetermined landmarks on the surface of the asteroid. Retina is derived from the stereophotoclinometry (SPC) methods developed by Gaskell,[3] which have a rich heritage on several planetary and small-body missions such as Voyager's exploration of Io,[4] NEAR Shoemaker,[5] Hayabusa,[6] Rosetta,[7,8] Dawn,[9,10] and others. Reference 11 gives additional details of the Retina design and ARRM mission.

This paper characterizes the performance of these SPC-derived landmark template matching algorithms when subjected to a variety of navigational and model error sources that are important during the vehicle's descent to the surface. This study is performed as part of an effort to develop requirements for the onboard GN&C hardware and software, and to validate assumptions (*e.g.*, measurement noise statistics) that are being used to develop the descent GN&C concept of operations. Furthermore, in the process of evaluating the performance of this landmark measurement system, we have developed several improvements to the original methodology that will eventually be incorporated into the Retina flight software version of this system.

SPC is the process of estimating terrain slopes and surface brightness (*i.e.*, albedo) from images. More specifically, at a given point on the surface of the body, three parameters are solved for: the slope in two directions and the albedo. Once the slopes are computed, they can be integrated to give the terrain heights, resulting in a digital elevation map (DEM) of the planetary or small-body surface. Additional data such as limb measurements are used to constrain the slope integrations. SPC is accomplished using a set of images; for a given surface point, the SPC solution requires at least three images of varying geometry and lighting in which the point appears, but in practice many more images (10s to 100s) are used to solve for the slopes and albedo in a least-squares sense.

SPC requires knowledge of the spacecraft and camera state, hence it is not a simultaneous localization and mapping method. Instead, SPC is usually performed iteratively in conjunction with a ground-based navigation process, *i.e.*, as the vehicle slowly approaches the target body, the ground-based navigation will estimate the target-relative navigation state, which is then fed into SPC to solve for a DEM of a certain spatial resolution. Once the DEM is available from SPC, an image registration process called "autoregister" is performed on the ground to compare navigation images with the pre-computed DEM data to obtain LOS measurements to landmarks within the DEM. As these terrain-relative LOS measurements become available, they can be fed into the navigation system to further refine the spacecraft state estimate, and the cycle repeats as the spacecraft approaches the body and higher-resolution images are obtained. The autoregister process is analogous to the registration performed in other applications such as processing of geospatial remote sensing data, *i.e.*, the alignment (or registering) of collected imagery with a DEM on the Earth.[12] In the context of SPC and autoregister, the LOS measurement to a specified landmark is generated by solving for the shift that best aligns a collected image of a landmark with its DEM. In other words, the DEM is assumed to be known to the navigation system, and collected imagery is compared with the DEM to produce LOS measurements to landmarks. Note that for the above-mentioned missions that have used SPC and autoregister in the past, both of these processes have been performed on the ground.

The ARRM concept of operations (conops) assumes a similar strategy for SPC to be performed on the ground, but one innovation is the planned application of the autoregister functionality onboard the vehicle. We are denoting this planned flight SW system for landmark measurements as Retina; the focus of this paper is a simulation of the autoregister-derived algorithms that will lead to Retina. JPL is separately incorporating the autoregister functionality for landmark-based navigation into

the AutoNAV flight SW system for onboard optical GN&C.[13] This version of autoregister, called OBIRON (Onboard Image Registration for Optical Navigation), was tested on the ground using both Hayabusa[6,13,14] and Dawn[15] imagery. In the case of Hayabusa, imagery of the descent from 740 to 57 m range to the surface was used for testing.[6] Reference 16 describes offline testing of OBIRON using aerial images from the Death Valley and Nevada Test Site in support of the Autonomous Landing and Hazard Avoidance Technology project with applications for a lunar landing. The planned ARRM conops for Retina is potentially the first time this SPC and autoregister functionality will be performed close to the surface of a small-body; the focus of the present paper is the range from 50 m from the surface.

DEFINITIONS AND TERMINOLOGY

It is useful to first define some terminology and variables used in the SPC and landmark template matching process before describing the overall conops flow. The reference frame $\mathcal{F}_b$ is the target asteroid's body-fixed frame (see Figure 1). The asteroid surface map is divided into a series of *maplets* that tile the surface (with partial overlaps allowed). The SPC literature sometimes refers to maplets as "L-maps" as well.[3] Below is a list of some of the properties of a maplet, all of which are defined in the maplet creation process of SPC:

- Landmark – the center (origin) of a given maplet is denoted as a *landmark*, with a position vector $\mathbf{r}_{lm}$ relative to the target body. Note that the landmark itself does not have to be a distinguishing feature, such as a boulder or crater; it is the surrounding maplet terrain's height and albedo that form our required image templates. In other words, the maplet terrain itself must have a certain amount of variation.

- Maplet Frame – the local coordinate frame centered on the landmark, $\mathcal{F}_m$, where the z-axis points towards zenith. The orientation of $\mathcal{F}_m$ relative to $\mathcal{F}_b$ is known.

- Maplet Grid Resolution and Scale – the number of grid elements that define the maplet (*i.e.*, $N \times N$), and the scale of each maplet grid element (*i.e.*, meters per element). Note that the term "maplet pixel" is sometimes used as well to describe a maplet grid element, but can cause confusion with image pixels.

- Maplet Space Coordinate - the cartesian position $\mathbf{r} = (x, y, z)$ that describes a point in the maplet $\mathcal{F}_m$.

- Height – an $N \times N$ matrix of height values that is a function $z = z(x, y)$ of planar grid coordinates in $\mathcal{F}_m$.

- Relative Albedo– an $N \times N$ matrix of albedo values, also a function $a = a(x, y)$ of maplet planar grid coordinates in $\mathcal{F}_m$.

The albedo contained in the maplet is not an absolute albedo; it is a relative albedo because it is a description of a given maplet element's surface material brightness relative to that of all other elements in that maplet. For example, if points A and B in a maplet have $a(x_A, y_A) = 1$ and $a(x_B, y_B) = 2$, then point B is twice as bright as point A (assuming they have equal slopes and Sun-observer geometry). Hence, the relative albedo is only meaningful when used with the assumed illumination model, discussed below. In the SPC maplet construction process, the relative albedo is

solved on a maplet-by-maplet basis; the relative albedo alone cannot be compared across maplets as a description of the inherent surface brightness.

Figure 2 shows an example of the height and relative albedo stored in one of the maplets used in this study, where the number "Bxxxxx" is an identifier for this set of maplets. Here we use $N = 99$, as is common in other SPC applications. Larger maplets (*i.e.*, larger values of N) are possible, but the number of computations increases with maplet size, which is a concern for a flight SW application. The process for generating the synthetic maplets used in this study is described later.
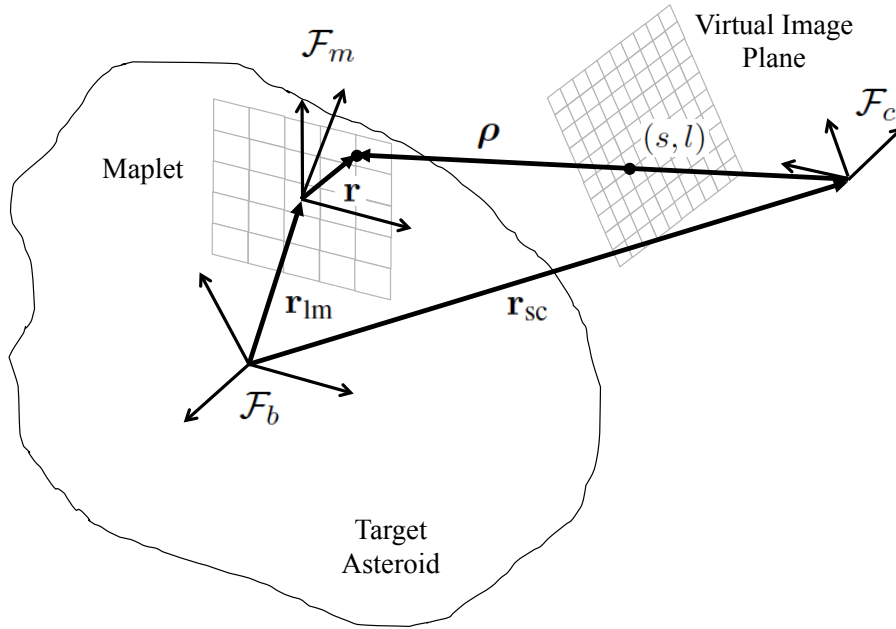

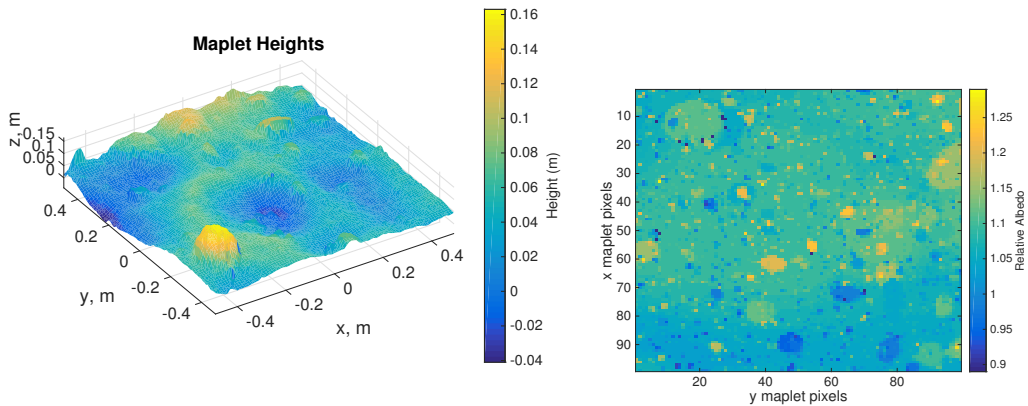**Figure 1**: Illustration of reference frames and vectors for landmark measurements.

Figure 2: Example height and relative albedo stored in a maplet, from B02246.

4

Transformation from Maplet Space to Image Space

Figure 1 shows the vector relationship

$$\mathbf{r}_{\text{lm}} + \mathbf{r} - \mathbf{r}_{\text{sc}} = \boldsymbol{\rho} \tag{1}$$

where $\mathbf{r}_{\text{sc}}$ is the spacecraft position vector relative to the $\mathcal{F}_b$ origin, and $\boldsymbol{\rho}$ is the position vector of a surface point in the maplet relative to the camera focal point centered on the camera frame $\mathcal{F}_c$. Note that in the remainder of this study, we ignore the offset of the camera relative to the spacecraft body center. Also, we ignore errors in knowledge of the camera position and orientation relative to the spacecraft, and in essence treat the spacecraft as consisting of nothing but the camera. The LOS vector to a surface point is then $\hat{\boldsymbol{\rho}} = \boldsymbol{\rho}/||\boldsymbol{\rho}||$. Considering a virtual image plane in front of the focal point, then the point of intersection between $\hat{\boldsymbol{\rho}}$ and this plane is described by image space coordinates (s, l), which are the (sample,line) coordinates in the image*.

The optical model follows Reference 17. The nonlinear measurement model that describes the (s, l) measurements to a surface point $\mathbf{r} = (x, y, z)$ as a function of the spacecraft pose $\mathbf{x}$ (*i.e.*, position and attitude), modeled landmark position $\mathbf{r}_{\text{lm}}$, and vector of camera model parameters $\mathbf{c}$ is denoted

$$\begin{bmatrix} s \\ l \end{bmatrix} = h(\mathbf{x}, \mathbf{r}_{\text{lm}}, \mathbf{c}) \tag{2}$$

In other words, $h()$ is the transformation that maps a point in maplet space to a point in image space. The steps involved in Eq. 2 are as follows. The position vectors in Eq. 1 are initially expressed in $\mathcal{F}_b$,

$$\mathbf{r}_{\text{lm}}^b + \mathbf{r}^b - \mathbf{r}_{\text{sc}}^b = \boldsymbol{\rho}^b \tag{3}$$

The vector $\boldsymbol{\rho}^b$ is then rotated into $\mathcal{F}_c$ using the assumed camera attitude knowledge between $\mathcal{F}_b$ and $\mathcal{F}_c$:

$$\boldsymbol{\rho}^c = \mathbf{R}^{b \to c} \boldsymbol{\rho}^b \tag{4}$$

The 2D gnomonic projection (*i.e.*, pinhole camera model) gives the coordinates $\mathbf{z} = \begin{bmatrix} z_x & z_y \end{bmatrix}^T$ in mm on the virtual image plane:

$$\mathbf{z} = \frac{f}{\rho_3^c} \begin{bmatrix} \rho_1^c \\ \rho_2^c \end{bmatrix} \tag{5}$$

where f is the focal length and $\boldsymbol{\rho}^c = \begin{bmatrix} \rho_1^c & \rho_2^c & \rho_3^c \end{bmatrix}^T$. A model for geometrical distortion (*i.e.*, deviations from a simple pinhole camera optical model) is then applied:

$$\mathbf{z}' = \mathbf{z} + \begin{bmatrix} -z_y r & z_x r^2 & -z_y r^3 & z_x r^4 & z_x z_y & z_x^2 \\ z_x r & z_y r^2 & z_x r^3 & z_y r^4 & z_y^2 & z_x z_y \end{bmatrix} \boldsymbol{\epsilon} \tag{6}$$

where $r = ||\mathbf{z}||$, and $\boldsymbol{\epsilon} = \begin{bmatrix} \epsilon_1 & \cdots & \epsilon_6 \end{bmatrix}^T$ are the parameters that describe the distortion due to 2nd-order radial distortion and tangential distortion. The coordinates on the distorted virtual image plane $\mathbf{z}' = \begin{bmatrix} z_x' & z_y' \end{bmatrix}^T$ are still expressed in mm; the mapping to pixel coordinates (s, l) is achieved with

$$\begin{bmatrix} s \\ l \end{bmatrix} = \mathbf{K} \begin{bmatrix} \mathbf{z}' \\ 1 \end{bmatrix} \tag{7}$$

---

*The (sample,line) measurements are synonymous with the (column,row) notation for describing the pixel coordinates in a image.

where the matrix

$$\mathbf{K} = \begin{bmatrix} K_x & K_{xy} & s_0 \\ K_{yx} & K_y & l_0 \end{bmatrix} \tag{8}$$

contains the image pixel coordinates of the principle point (s_0, l_0) (*i.e.*, where the camera boresight intersects the image plane), the terms K_x and K_y convert from units of mm to pixels, and the terms K_{xy} and K_{yx} apply a rotation. We can now define the vector of camera model parameters in Eq. 2 as $\mathbf{c} = (f, \epsilon, \mathbf{K})$.

PROCESS OVERVIEW

This section describes the overall optical navigation process in conjunction with the TRN phase of the mission (see Figure 3). The major components in the landmark template matching process are described in the following subsections. This paper does not go into detail on the other elements of the planned onboard GN&C process, such as the filter, controller, guidance algorithms, and state propagation.
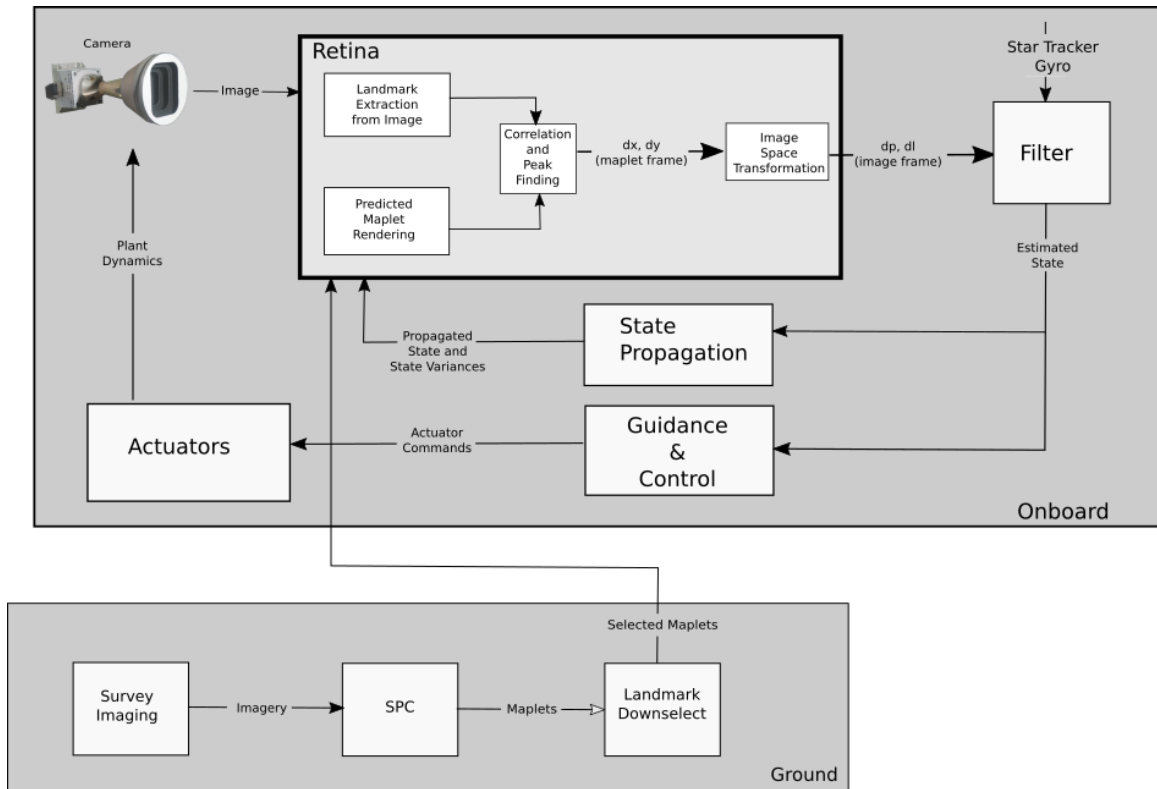

Figure 3: Flow chart of SPC, Retina, and optical GN&C processes.

The ground-based SPC functionality shown in Figure 3 is assumed to be nearly identical to the system used in previous SPC missions, as discussed above in the introduction. One set of inputs to the ground-based SPC is the narrow field-of-view (FOV) survey images taken from a higher mapping altitude. The outputs of the SPC process are the individual maplets. Furthermore, the ground system will include a landmark down-selection algorithm responsible for taking the predicted spacecraft ephemeris and attitude pointing and choosing the appropriate L-maps to be uploaded to the

vehicle.

The inputs to the landmark template matching process are: the maplets generated during the ground-based SPC process, the predicted spacecraft state at the current time from the onboard GN&C subsystem, and the current wide-FOV imagery from the onboard optical navigation camera. The landmark template matching is usually performed in an iterative fashion, where an initial guess of the landmark LOS vector is refined. For the initial iteration into the template matching loop ($i = 0$), an initial estimate of the (s, l) measurement to the landmark is computed using the *a priori* pose estimate $\mathbf{x}^*$ and the model from Eq. 2:

$$\begin{bmatrix} s \\ l \end{bmatrix}_{i=0} = h(\mathbf{x}^*, \mathbf{r}_{\mathrm{lm}}, \mathbf{c}) \tag{9}$$

Landmark Extraction from Image

In this step, the portion of the image that contains the maplet data is identified, and those image pixels are transformed from image space into maplet space, *i.e.*, the maplet data is *extracted* from the image. The main steps for accomplishing the image extraction are as follows:

- Compute the Jacobian of $h()$ with respect to $\mathbf{r}$ evaluated on $(\mathbf{x}^*, \mathbf{r}_{\mathrm{lm}}, \mathbf{c})$ using finite differencing:

$$\mathbf{H} = \left. \frac{\partial h()}{\partial \mathbf{r}} \right|_{(\mathbf{x}^*, \mathbf{r}_{\mathrm{lm}}, \mathbf{c})} \tag{10}$$

- Loop over each point $\mathbf{r}_k$ in maplet space, where $k \in \{1, \cdots, N^2\}$, and project that point into image space (s, l) using the linearization

$$\begin{bmatrix} s \\ l \end{bmatrix}_k = \begin{bmatrix} s \\ l \end{bmatrix}_i + \mathbf{H}\mathbf{r}_k \tag{11}$$

- The image data must be interpolated at the projected point, because the projected point in image space almost certainly will not fall exactly on an image pixel (recall Figure 1). This image interpolation is nominally performed with bilinear interpolation.

- Iterate around the maplet point $\mathbf{r}_k$ using a small search distance, and for each of these additional points in maplet space, repeat the above-mentioned projection and interpolation steps. The purpose of this additional iteration is to perform local averaging of the computed brightness.

- Loop over each point in the extracted image and normalize the brightness within the maximum detector thresholds. Denote the final extracted image intensity at maplet coordinate k as $I_{\mathrm{ext}}(k)$. See Figure 4a for an example of an extracted maplet image, where the color scale denotes the normalized image intensity.

Predicted Maplet Rendering

The L-map data is illuminated using knowledge of the slope and albedo at each point, as well as the sun direction and assumed spacecraft pose. This predicted brightness I at each point k in the L-map is calculated using an illumination model that has been developed over the years for airless
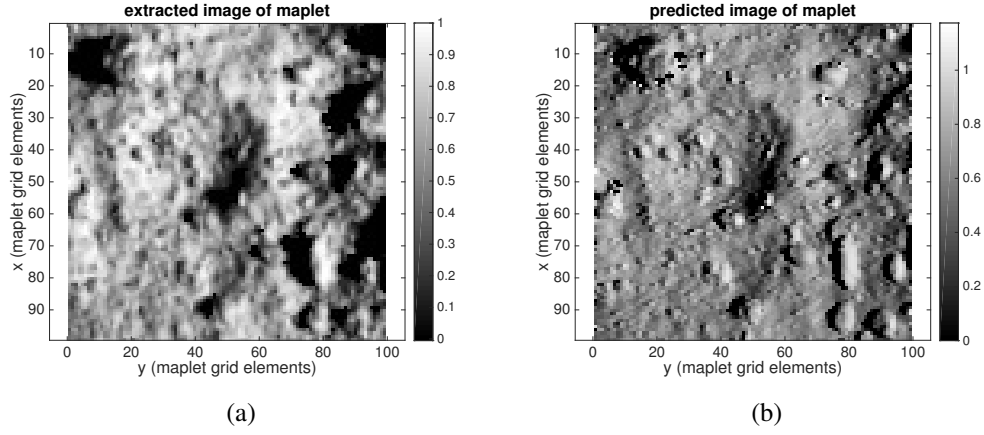
Figure 4: Left (a) example of extracted maplet image from L-map B02246, right (b) example of predicted maplet image from L-map B02246.

planetary bodies. Let $\hat{s}$ denote the sun direction unit vector in $\mathcal{F}_m$, and let $\hat{e}$ denote the emission direction unit vector in $\mathcal{F}_m$ (*i.e.*, the direction from the surface to the observer). Let the surface normal vector at $\mathbf{r}$ in $\mathcal{F}_m$ be $\hat{n}$. Then the incidence angle, emission angle, and phase angle are given respectively with

$$i = \cos^{-1}(\hat{s} \cdot \hat{n}) \tag{12}$$

$$e = \cos^{-1}(\hat{e} \cdot \hat{n}) \tag{13}$$

$$\alpha = \cos^{-1}(\hat{s} \cdot \hat{e}) \tag{14}$$

The function to calculate the predicted brightness at maplet coordinate $\mathbf{r}_k$ is[3]

$$I_{\text{pred}}(k) = \Lambda a(x_k, y_k) R(\cos i, \cos e, \alpha) + \Phi \tag{15}$$

where Λ is an image scaling multiplier, $a(x_k, y_k)$ is the relative albedo defined previously, Φ is a positive background term that can be used when there is background or haze in an image (*e.g.*, due to ambient lighting on a planet containing an atmosphere[16]), and R is the so-called "Lunar-Lambert" function defined as:[18]

$$R(\cos i, \cos e, \alpha) = (1 - L(\alpha)) \cos i + \frac{L(\alpha) \cos i}{\cos i + \cos e} \tag{16}$$

where the term $L(\alpha)$ is defined shortly. The Lunar-Lambert function is a combination of Lambert and Lommel-Seeliger reflectance functions, and is a simple model of single and multiple scattering, in which the scattering is isotropic. The term $L(\alpha)$ is a phase adjustment term to model limb-darkening. Reference 19 empircally models $L(\alpha)$ by fitting lunar data to a 3rd order polynomial. However, we follow the convention of Gaskell[3] which does an additional fit using an exponential as follows:

$$L(\alpha) = \exp(-\alpha/60) \tag{17}$$

where α is expressed in degrees. Note that the limb-darkening term $L(\alpha)$ is the only phase-dependent term in the intensity calculation. The Lunar-Lambert function of Eq. 16 has been validated on powdery materials in the laboratory, as well as disk-integrated properties of asteroids and natural satellites,[18] not to mention the flight programs where SPC has been used in the past.

The steps for computing the predicted maplet brightness are as follows:

8

- Given the current spacecraft state in $\mathcal{F}_b$, compute the following vectors in $\mathcal{F}_m$: sun unit vector ($\hat{s}$), and unit vector from maplet center to camera ($\hat{e}$). Note that the simplification is made where $\hat{e}$ is assigned to be the same for all points in the maplet, and to take on the value from the maplet origin.

- Because the maplet contains the height data and not the slope data, the slope must be computed from the height. This is done by looping over each point in the maplet and computing the slope in two directions with a finite differencing.

- Also in the loop over all points in the maplet, the illumination is calculated with Eq. 15. The result is the predicted illuminated maplet in $\mathcal{F}_m$.

The illumination model used for the predicted images for this version of the landmark template matching does not realistically account for shadowing, *i.e.*, a full-fledged ray tracing is not performed. Instead, in the interest of computational speed, a maplet pixel is calculated as being dark only if its incidence angle is greater than 90 degrees. This shadow modeling difference can be seen by comparing Figures 4a and 4b. This approximation is a hold-over from the original SPC and autoregister formulation, and its speed makes it desired for onboard image rendering. The implications of this modeling approach on the correlation step, as well as future enhancements to this methodology, are discussed below.

Correlation and Peak Finding

This step attempts to solve for the translational shift in maplet space $\Delta \mathbf{r}_i = (\Delta x, \Delta y)$ that maximizes the correlation between the predicted and extracted maplet images, where i is the current iteration of the template matching loop. If the onboard maplets contained no model errors and perfectly represented the true terrain, and if the camera model contained no errors, then only navigational offsets (*i.e.*, differences between the true and assumed spacecraft pose) would be responsible for non-zero values of $\Delta \mathbf{r}_i$ in this correlation step. By solving for the shift $\Delta \mathbf{r}_i$ using our *a priori* knowledge of the spacecraft pose, we can adjust our *a priori* knowledge of the LOS vectors to the landmarks.

Figure 5a is a simplified illustration of the process for correlating the predicted and extracted maplets. In this simple example for easy visualization, the maplet has dimensions of 5×5 maplet pixels, and the correlation search is performed over a 3×3 grid. The predicted maplet is depicted in blue, the extracted maplet is depicted in yellow, and the overlapping regions are shown in green. The correlator is looped over the maplet-space planar search dimensions $(\Delta x, \Delta y)$, and for a given value of overlap, a correlation metric is computed and stored in a matrix as shown. The correlation metric currently used is simply a linear correlation coefficient (i.e. the Pearson product moment coefficient):

$$\rho = \frac{\sum I_{\text{ext}} I_{\text{pred}} - \sum I_{\text{ext}} \sum I_{\text{pred}}}{\sqrt{\left[M \sum I_{\text{ext}}^2 - \left(\sum I_{\text{ext}} \right)^2 \right] \left[M \sum I_{\text{pred}}^2 - \left(\sum I_{\text{pred}} \right)^2 \right]}} \tag{18}$$

where M is the length of both signals I_{ext} and I_{pred}. The correlation coefficient ρ is defined from -1 (perfect inverse correlation) to 1 (perfect correlation).

Once the correlator loop has fully populated the correlation matrix, a peak correlation value is found. The peak is found by selecting points on both sides of the max and finding the intersection
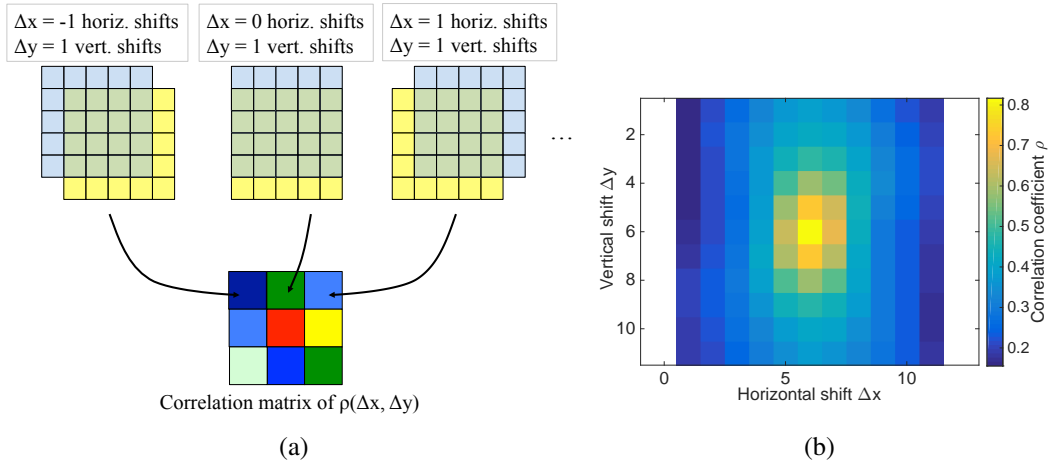
Figure 5: Left (a) shows a simplified illustration of the process for populating the correlation matrix $\rho(\Delta x, \Delta y)$. Right (b) is an example of the ρ matrix using I_{pred} and I_{ext} from our descent simulations.

of lines constructed from those points, where the slopes of the lines are computed from the correlation matrix gradient. The solution $\Delta \mathbf{r}_i$ is the shift that maximizes the correlation coefficient. The correlation search distances are controlled by the template matching loop iteration, e.g. $\Delta x = 5L_i$, where L_i in the current simulations begins at a max of 10 and decrements to 1. Hence, the search is initially performed over a larger area in maplet space and should converge to a small area. Note that the peak finding in the ρ matrix allows sub-maplet-pixel solutions for $\Delta \mathbf{r}_i$. Figure 5b is an example of the ρ correlation matrix using the predicted and extracted maplets (from an unperturbed case) from our ARRM descent simulations, where the correlation matrix has dimensions of 11×11.

It is important to note that the correlated images from the predicted and extracted maplets are decomposed into a one-dimensional signal, hence all spatial information is lost, and the correlation is performed on a pixel-by-pixel basis. Also, because the illumination model for the predicted maplets is known to be deficient with regard to shadow calculations (as mentioned above), a pair of image pixels from the predicted and extracted maplets is included in the correlation signal only if both are greater than a near-zero threshold. In other words, the correlator is intentionally disregarding shadowed pixels in either image. Lastly, the linear correlation coefficient ρ is invariant to linear transformations of one signal relative to the other; for example, the slight differences in the normalized image intensities between I_{ext} and I_{pred} apparent in the color scales in Figures 4a and 4b do not affect ρ.

Image Space Transformation

Lastly, the landmark LOS shift measurements are transformed from maplet space into image space, again using the *a priori* spacecraft state knowledge. Here, the linearized transformation is used again:

$$\begin{bmatrix} s \\ l \end{bmatrix}_{i+1} = \begin{bmatrix} s \\ l \end{bmatrix}_i + \mathbf{H} \Delta \mathbf{r}_i \tag{19}$$

If the template matching loop is done with all iterations i, then the final landmark LOS measurements (s, l) can be fed into the onboard GN&C filter, otherwise the loop repeats.

10

SIMULATION ENVIRONMENT

An in-house renderer called Geomod is used to model the 3D scene geometry, lighting models, and ray tracing for synthesizing the "truth" images in our ARRM simulations. The ray tracer uses Monte Carlo importance sampling to follow a large number of incoming light ray directions (backwards) from a pixelated detector grid, through a lens system, and into a scene. It is physically-based on radiometric light transport, geometric optics, and statistically unbiased Monte Carlo integration. Geomod has been used previously to support simulations of the Origins, Spectral Interpretation, Resource Identification, Security, Regolith Explorer (OSIRIS-REx) mission.

For the purposes of this study, the wide-FOV navigation camera is baselined using similar parameters as the NAVCAM wide-FOV camera on OSIRIS-REx (see Table 1). From Table 1, the principle point pixel coordinates are $(s_0, l_0) = (1296.5, 972.5)$, and $K_x = 454.54$, $K_y = -454.54$, and $K_{xy} = K_{yx} = 0$.

Table 1: Wide-FOV camera parameters used in this study

Parameter	Value
Detector horizontal resolution	2592 pixels
Detector vertical resolution	1944 pixels
Focal length, f	7.68 mm
Detector pixel dimensions	2.2×2.2 microns
Camera horizontal FOV	40.7 deg
Camera vertical FOV	31.1 deg

There are two sets of maplets for the asteroid surface used in this study. The first is the "truth" set used to render the synthetic images from Geomod, which has 3-mm resolution maplet pixels. The onboard maplet set (*i.e.*, the maplets we assume would be used onboard during the descent from 50-m altitude, denoted with the "B" prefix) is derived from the truth set for the purposes of this simulation*, but is down-sampled and smoothed to a final maplet pixel resolution of 1-cm, with $N = 99$. The down-sampling and smoothing from truth maplets to onboard maplets introduces small systematic errors (*e.g.*, on the order of a few cm in height).

The asteroid surface is simulated with a suite of FORTRAN algorithms provided by Gaskell, which take as input an approximate shape model and applies a stochastic interpolation to add a realistic distribution of surface boulder, craters, and accretion layer. Earlier examples of this methodology can be found in References 20 and 21. For example, the cratering distribution is based on a power law relating the number of craters and their diameters, as observed in nature. The output is a series of maplets at the desired resolution and scale. Gaskell[5] shows an example of the synthetic shape generation algorithms being applied to Bennu for the OSIRIS-REx mission. Figure 6 shows the synthesized asteroid surface within the FOV at 50 m altitude, with 12 landmarks indicated, where the magenta squares indicate the size of each individual maplet. Note that each maplet considered here is 1 m × 1 m, whereas the entire FOV at 50 m altitude covers an area on the surface of approximately 28 m × 37 m. Figure 7 shows the extracted maplet images for each of the 12 landmarks at 50 m altitude. The reference trajectory for the ARRM vehicle's descent to the surface is the same as that used in Reference 22. Note that our simulation of the landmark matching algorithms in the present paper is not a dynamic simulation that uses the landmark measurements in

---

*During actual operations, the onboard maplets come from the SPC process as described above, because obviously the truth terrain is unknown.

a closed loop; instead we simply use the vehicle's asteroid-relative state a given time to render the truth images and measure the landmarks.

PERFORMANCE CHARACTERIZATION

This section describes the results of running the landmark template matching algorithms when subjected to imperfect knowledge of the spacecraft navigational state and model parameters (*i.e.*, parameters affecting both the camera model and terrain model).

Perturbed cases at 50 m altitude

The nominal states and model parameters were perturbed at 50-m altitude from the surface as described in Table 2. Each perturbation is zero-mean and normally distributed with the 1-σ standard deviations shown. Most of the perturbation values in the table are realistic assumptions at this stage of the preliminary design, with the exception of the spacecraft pose knowledge relative to the asteroid, as discussed below. The landmark template matching algorithms were simulated in a Monte Carlo (MC) setting, with Latin Hypercube Sampling (LHS)[23] of 500 samples per landmark. LHS generally allows a more accurate representation of the desired probability density function compared
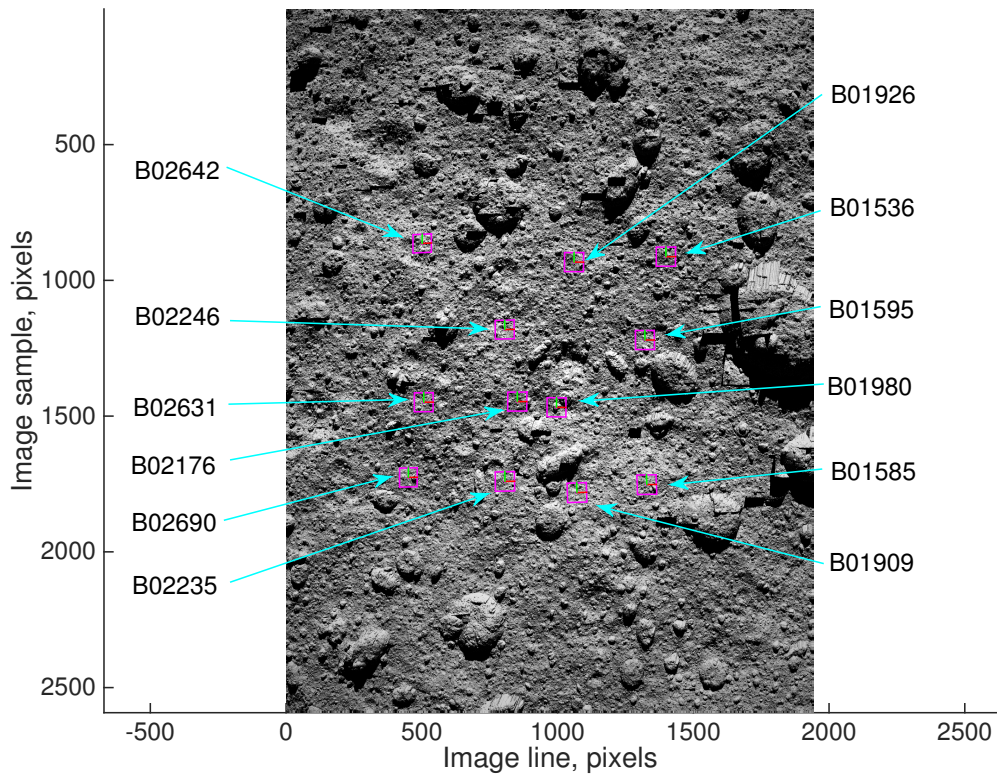

Figure 6: Synthetic image of asteroid surface from Geomod at 50-m altitude, showing location of the 12 landmarks used in the performance characterization.
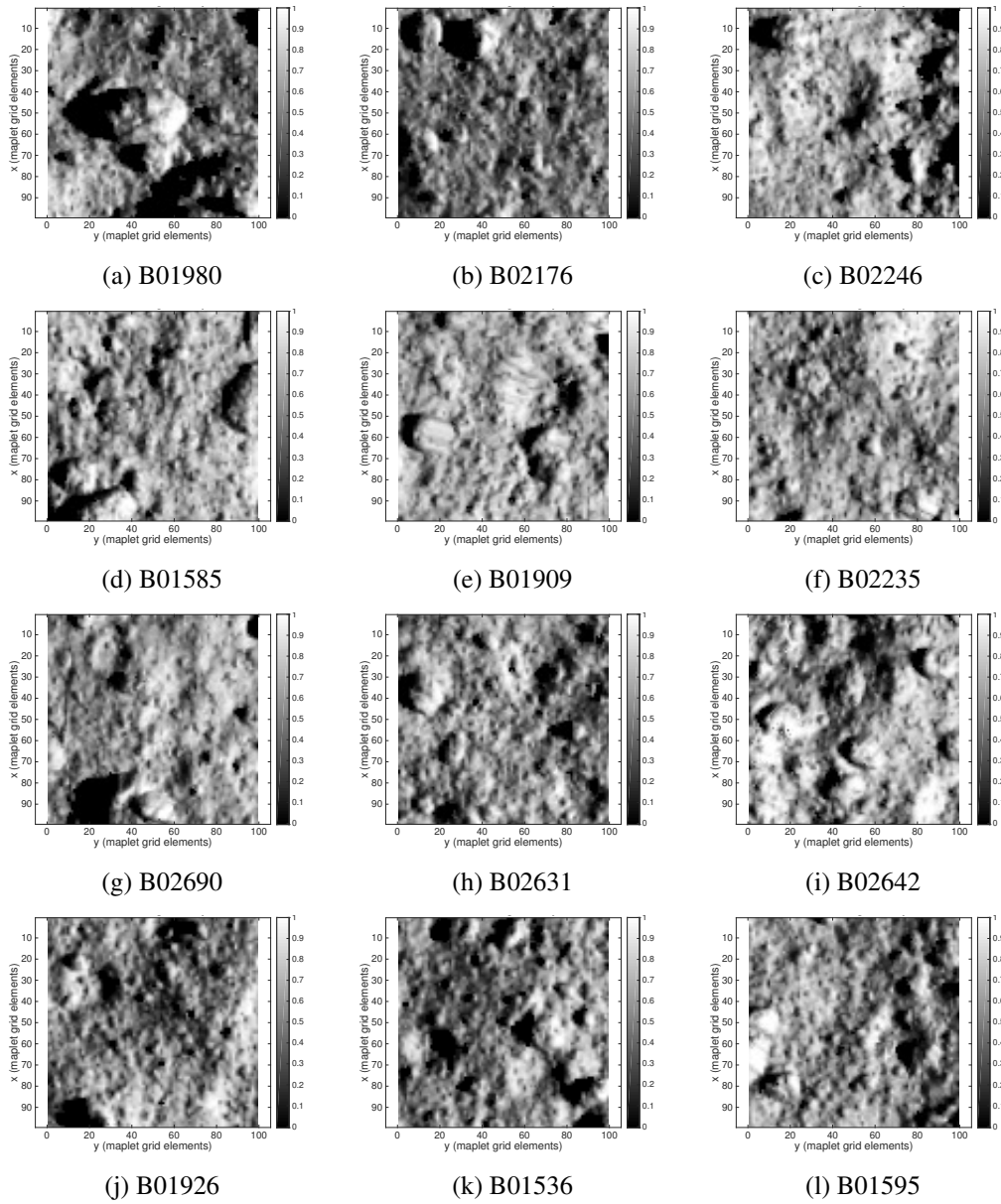
(a) B01980

(b) B02176

(c) B02246

(d) B01585

(e) B01909

(f) B02235

(g) B02690

(h) B02631

(i) B02642

(j) B01926

(k) B01536

(l) B01595

Figure 7: Extracted maplet images (I_{ext}) for the 12 L-maps at 50-m altitude.

with MC for the same number of samples. LHS was chosen because the landmark image processing algorithms are currently implemented in Matlab, hence a large number of MC samples require a long computation time. The "truth" measurement $(s, l)_{\text{truth}}$ is defined as Eq. 2 evaluated on the unperturbed values of $(\mathbf{x}, \mathbf{r}_{\text{lm}}, \mathbf{c})$, the "perturbed" $(s, l)_{\text{perturb}}$ is the result of the landmark template matching algorithms when $(\mathbf{x}, \mathbf{r}_{\text{lm}}, \mathbf{c})$ are perturbed, and the resulting errors in the measurement as a result of the perturbations are $(s, l)_{\text{err}} = (s, l)_{\text{truth}} - (s, l)_{\text{perturb}}$. Note that the synthesized images (simulated from the navigation camera) are not re-rendered for each perturbed sample due to the long computational time required; rather we are perturbing our knowledge of the navigation state

and model parameters for a single set of collected (*i.e.*, synthesized) images. Additional fidelity may be achieved in future simulations that also perturb the truth state (as well as rendered synthetic imagery).

Table 2: Monte Carlo Simulation Parameters

Parameter or state to perturb	1-σ std applied
Asteroid-relative spacecraft position $\mathbf{r}_{sc}$, each component	0.1667 m
Asteroid-relative spacecraft attitude, each component	0.05 deg
Asteroid-relative landmark position $\mathbf{r}_{lm}$, each component	3.33 cm
Maplet terrain height $z(x, y)$	3.33 mm
Maplet terrain albedo $a(x, y)$	0.047
Camera model pixel skew K_{yx}	1×10^{-5}
Camera model principle coordinates (s_0, l_0)	0.1667 pixels
Camera model focal length f	0.004 mm
Camera model distortion coefficients ϵ	$(1 \times 10^{-5}, 1 \times 10^{-7}, 1 \times 10^{-5}, 1 \times 10^{-5}, 0, 0)$
Asteroid-relative sun vector direction, RA and DEC	0.3 deg

The results of the LHS simulations are summarized in Table 3, and Figure 8 shows the distribution in $(s, l)_{\mathrm{err}}$ for each landmark. The first column in the table is the landmark ID number. The next four columns are the means and 1-σ standard deviations of $(s, l)_{\mathrm{error}}$. The 6th column shows the number of samples where a peak in the correlation matrix was not found, *e.g.*, due to the peak being on the edge of the search distance, or the correlation matrix not showing a clearly defined peak. The 7th column shows the number of samples where the peak correlation was found, but with a value below a specified threshold of 0.3. The threshold level was determined based on experience in the simulations, but this value is subject to change. The 8th column is the landmark template matching success rate, meaning the fraction of those 500 samples that successfully had a peak correlation value above the 0.3 threshold. The last column is the mean across the 500 samples of the max correlation value ρ from the correlation matrix from each sample. The samples shown in Figure 8 correspond to those having a successfully located correlation peak. From these results, it is clear that these 12 landmarks have a line error l_{err} mean close to zero, but a small bias of approximately -0.1 pixels in the sample error s_{err}. The error distributions shown in Figure 8 do not show any strong non-Guassian behavior. The l_{err} 1-σ std is consistently larger than the corresponding statistic in s_{err}, but both are below approximately 0.1 image pixels.

The biggest influences on the size of the errors $(s, l)_{\mathrm{err}}$ are the knowledge errors in spacecraft pose, followed to a lesser extent by $\mathbf{r}_{lm}$, (s_0, l_0), and $z(x, y)$. The majority of the failure cases in the landmark template matching (*i.e.*, the approximately 10% of the 500 samples for each landmark) are due to the spacecraft pose knowledge errors projecting the extracted maplet imagery too far off of the maplet terrain in maplet space. Recall from the discussion on the correlation in maplet space, that the correlation is only performed on the overlapping portions of the two signals. As the correlation signal size decreases, the quality of the linear correlation quickly degrades (especially in the presence of noise). Considering the 1-σ values, the spacecraft position alone is 0.17 m and the attitude is 0.05 deg; when these two act in the same direction (parallel to the asteroid surface) the result is an offset in the boresight intersection with the asteroid surface of roughly 42 cm at the 2-σ level. The max search distance used in the correlation loop for these tests is $L = 10$, corresponding to a maplet space max search distance of $5L = 50$ maplet pixels, or 50 cm. Hence, when the spacecraft pose knowledge errors approach the 2-σ levels, the correlation algorithm begins to approach its maplet space search distance limits when $L = 10$.
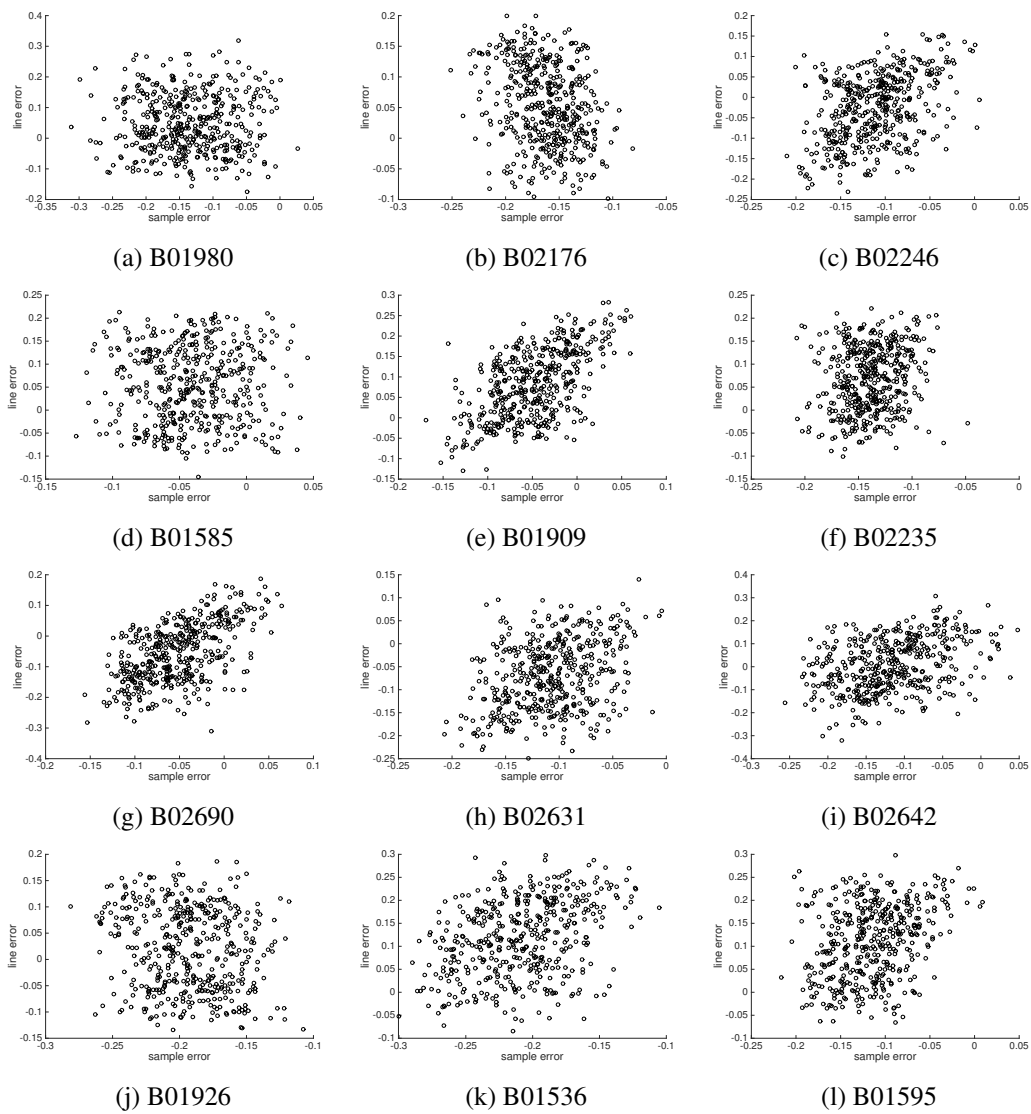
(a) B01980

(b) B02176

(c) B02246

(d) B01585

(e) B01909

(f) B02235

(g) B02690

(h) B02631

(i) B02642

(j) B01926

(k) B01536

(l) B01595

Figure 8: Monte Carlo results from several landmarks at 50-m altitude, where the axes are $(s, l)_{\mathrm{err}}$ in units of image pixels.

Table 3: Summary of Monte Carlo (LHS) Simulation Results at 50 m altitude.

L-map ID	Sample error mean [pix]	Line error mean [pix]	Sample error std [pix]	Line error std [pix]	Num. not found	Num. below thresh.	Success Rate	Mean of max ρ
B01980	-0.136	0.048	0.062	0.096	42	15	0.89	0.54
B02176	-0.163	0.053	0.028	0.066	23	25	0.90	0.54
B02246	-0.111	-0.027	0.041	0.082	31	18	0.90	0.58
B01585	-0.041	0.054	0.033	0.082	36	20	0.89	0.56
B01909	-0.049	0.081	0.043	0.085	36	15	0.90	0.55
B02235	-0.139	0.068	0.025	0.071	39	12	0.90	0.55
B02690	-0.052	-0.056	0.043	0.097	52	16	0.86	0.57
B02631	-0.107	-0.069	0.038	0.076	37	13	0.90	0.57
B02642	-0.117	0.007	0.058	0.113	46	15	0.88	0.58
B01926	-0.193	0.019	0.032	0.078	49	6	0.89	0.59
B01536	-0.208	0.118	0.037	0.083	35	19	0.89	0.58
B01595	-0.114	0.111	0.041	0.080	33	25	0.88	0.57

The descent GN&C conops currently assumes the spacecraft pose navigational errors to be approximately 0.5 m and 0.6 deg (3σ) in each component at 50 m altitude, based on a linear covariance analysis assuming landmark measurements (s, l) with 1σ noise of 1 pixel.[22] Thus, we have shown that the achievable landmark measurement noise may be smaller, but we have also assumed a smaller navigational error in attitude knowledge (recall Table 2). Thus, the current landmark template matching algorithm and settings may be insufficient for accurately providing landmark measurements with this level of spacecraft pose error, which requires further investigation. One alternative is to increase the search distance L: the downside of this approach is the potential increase in computational burden as a larger search area must be iterated in the correlator. Another alternative is to increase the maplet template size (*i.e.*, N), which comes with its own increase in computation burden because many of the calculation are performed on a pixel-by-pixel basis in the maplet. We are exploring a new approach to solving this problem by performing the correlations in image space, as opposed to maplet space, described below in the discussion on Retina.

Perturbed cases during descent below 50-m altitude

The above perturbed cases were repeated for three landmarks at 30-second intervals during the descent, beginning at 50-m altitude and stopping before 25-m altitude. Figure 9 shows these results, where the mean and 1-σ std from each 500-sample LHS run are shown as a box-and-whiskers plot. The sample and line errors are shown in black and blue, respectively. Note that each run of the landmark template matching algorithm at a given instant is independent, *i.e.*, the (s, l) solution at one time step is not used as an input to the next time step. Only three landmarks are shown here because of the large number of samples required to run the LHS simulations at this 30-second time step in Matlab. Figure 9 shows that the standard deviations do not increase greatly as the spacecraft approaches the surface. The largest increase here is the sample error mean and std for L-map B01980, which nearly double during the approach. Figure 7 shows that this landmark has two large boulders, unlike L-maps B02176 and B02246, and the boulder shadows exist mostly along the sample direction. One possible explanation for this error growth is mis-modeling of the boulder shadows in the predicted image (as described after Eq. 17). Lastly, it is worth noting that neither the landmark template matching success rate nor the max correlation value changed significantly over the altitude ranges tested.
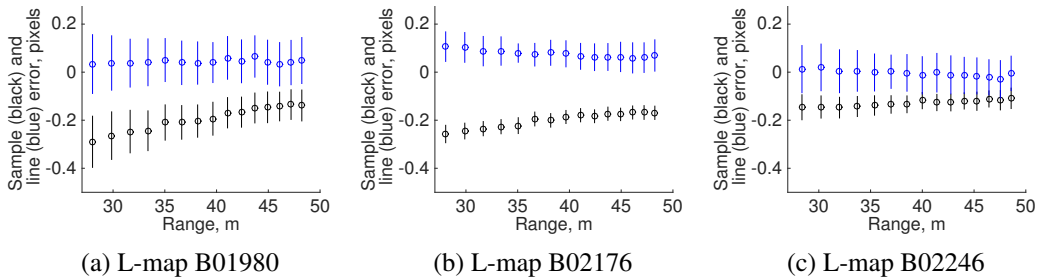
$$\text{(a) L-map B01980} \qquad \text{(b) L-map B02176} \qquad \text{(c) L-map B02246}$$

Figure 9: Mean and 1-σ std results for $(s, l)_{\text{err}}$ for three landmarks at 30-second intervals during descent from 50 to 25 m range.

FUTURE RETINA DEVELOPMENT

As discussed above, the maplet-space correlations that form the basis of the pre-existing landmark template matching algorithms are limited when the spacecraft pose knowledge errors result in poor correlations or insufficient overlapping data. One approach we are taking with our Retina fight software development is to instead project the maplet data into image-space and perform the correlations there. A benefit of this approach is that a larger amount of image data is available in the FOV as the correlation search distance is extended beyond the geometric limits of the maplet. In other words, we are comparing the maplet data with additional regions in the image around the assumed maplet, as opposed to maplet-space searches where large search distances can result in very little overlapping data (or no overlapping data in the extreme). Recall from Figure 6 that each maplet only occupies a fraction of the overall FOV. Hence, the Retina approach of correlating in image space may be more robust to spacecraft pose knowledge errors, although it is possible that the correlation search time could be large if the true landmark location in the image is much farther than expected. Another philosophical difference between Retina's image-space correlations and the SPC-derived template matching in maplet-space is that Retina does not modify the processed sensor data, and instead does the manipulations on the model-based maplet terrain data. Furthermore, a more realistic ray-tracing method is used for shadow modeling than the simple incidence angle check in the existing landmark template matching; this improved image predicting should allow more surface data to be included in the correlations and improve accuracy. Figure 10 shows some preliminary results of our new Retina algorithms for landmark template matching, under a similar MC setup as described above at 50-m (with nearly identical perturbations to spacecraft navigational states and model knowledge). It is clear that the mean errors are slightly improved and the standard deviations are somewhat larger; the big improvement is that these MC runs found 100% of the landmarks, versus the approximately 90% success rate in the existing algorithms. Additional information on planned Retina development can be found in Reference 11.

CONCLUSIONS

This work has demonstrated the SPC-derived landmark template matching algorithms during part of the descent below 50-m altitude above a simulated asteroid surface. The algorithms were shown to produce line-of-sight measurements to the specified landmarks with sufficient accuracy, assuming a low level of navigational error in the spacecraft's asteroid-relative pose. However, for larger navigational errors, this work has illustrated some fundamental limitations in the maplet-space correlations used in the existing landmark template matching algorithms. Preliminary results were

presented on a different algorithmic approach, where terrain data is projected into image-space for more robust correlation. This different approach to landmark template matching is being developed as the Retina flight software for eventual onboard implementation.
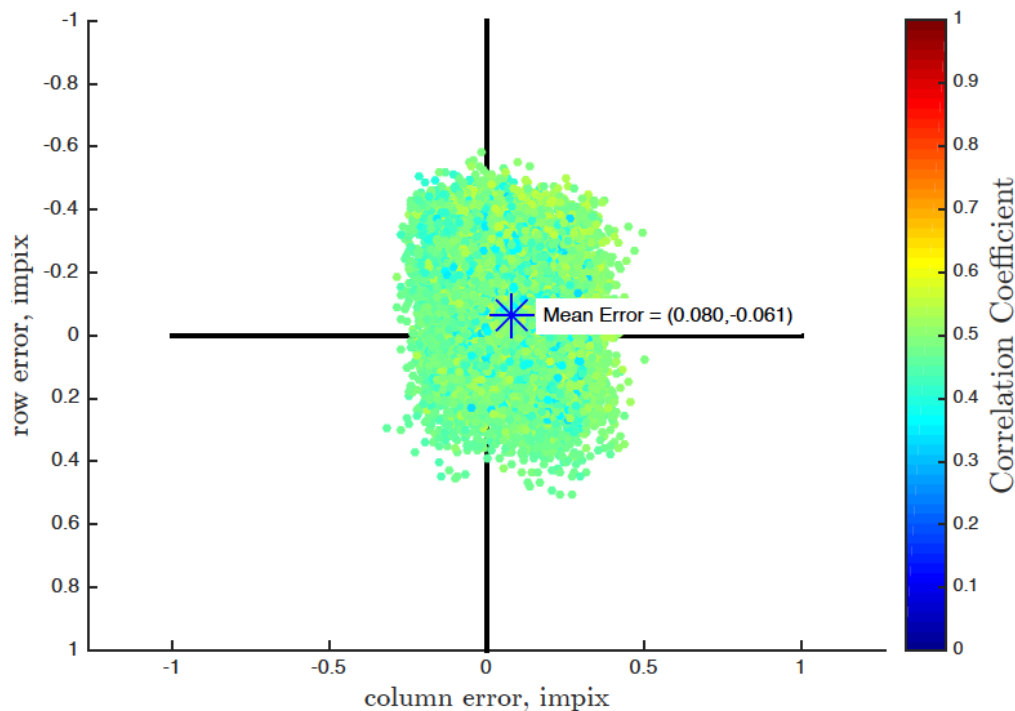

Figure 10: Example Monte Carlo results from Retina, where column = sample and row = line.

ACKNOWLEDGEMENTS

NOTATION

a	maplet relative albedo
$\mathbf{c}$	vector of camera model parameters
$\hat{e}$	emission direction unit vector
e	emission angle
$\mathcal{F}_b$	asteroid body-fixed frame
$\mathcal{F}_c$	camera frame
$\mathcal{F}_m$	maplet frame
f	camera focal length
$\mathbf{H}$	Jacobian of $h()$

$h()$ maplet-space to image-space transformation

I_{ext} extracted image intensity

I_{pred} predicted image intensity

i (subscript)   index of landmark matching loop

i incidence angle

$\mathbf{K}$ camera intrinsic matrix

K_x, K_y camera mm-to-pixel scaling terms

K_{xy}, K_{yx} camera image rotation terms

k (subscript)   index of discrete point in maplet

L correlation search distance

$L(\alpha)$ limb-darkening phase adjustment term

M length of vectors for correlation

N number of maplet grid elements per side

$\hat{n}$ surface normal direction unit vector

l line image coordinate, pixel

l_0 line image coordinate of principle point, pixel

$\mathbf{R}^{\text{b}\to\text{c}}$ rotation matrix from $\mathcal{F}_b$ to $\mathcal{F}_c$

R Lunar-Lambert function

$\mathbf{r}$ position of point in maplet

$\mathbf{r}_{\text{lm}}$ position of landmark

$\mathbf{r}_{\text{sc}}$ position of spacecraft

$\Delta\mathbf{r}$ solve-for shift in maplet space

r magnitude of $\mathbf{z}$

$\hat{s}$ sun direction unit vector

s sample image coordinate, pixel

s_0 sample image coordinate of principle point, pixel

$\mathbf{x}$ spacecraft pose

x, y cartesian coordinates within maplet

$\Delta x, \Delta y$ cartesian components of $\Delta\mathbf{r}$

$\mathbf{z}$ virtual image plane coordinates

$\mathbf{z}'$ distorted virtual image plane coordinates

z maplet height

z_x, z_y components of $\mathbf{z}$

α phase angle

$\boldsymbol{\epsilon}$ vector of camera distortion coefficients

Λ image scaling multiplier

$\boldsymbol{\rho}$ range vector from camera to surface point

ρ correlation value

ρ_1, ρ_2, ρ_3 components of $\boldsymbol{\rho}$

Φ positive background term

REFERENCES

[1] R. Merrill, M. Qu, M. Vavrina, J. Englander, and C. Jones, "Interplanetary Trajectory Design for the Asteroid Robotic Redirect Mission Alternate Approach Trade Study," *AIAA/AAS Astrodynamics Specialist Conference, San Diego, CA*, 2014. AIAA 2014-4457.

[2] D. Reeves, B. Naasz, C. Wright, and A. Pini, "Proximity Operations for the Robotic Boulder Capture Option for the Asteroid Redirect Mission," *AIAA Space 2014 Conference and Exposition, 4-7 Aug. 2014, San Diego, CA*, 2014. AIAA 2014-4433.

[3] R. Gaskell *et al.*, "Characterizing and navigating small bodies with imaging data," *Meteoritics and Planetary Science*, Vol. 43, 2008, pp. 1049–1061.

[4] R. Gaskell, "Digital Identification of Cartographic Control Points," *Photogrammetric Engineering and Remote Sensing*, Vol. 54, 1988, pp. 723–727.

[5] R. Gaskell, "Optical Navigation Near Small Bodies," *Advances in the Astronautical Sciences* (M. K. Jah, Y. Guo, A. L. Bowes, and P. C. Lai, eds.), Vol. 140, 2011, pp. AAS 11–220.

[6] R. Gaskell, O. Barnouin-Jha, D. Scheeres, T. Mukai, N. Hirata, S. Abe, J. Saito, M. Ishiguro, T. Kubota, T. Hashimoto, J. Kawaguchi, M. Yoshikawa, K. Shirakawa, and T. Kominato, "Landmark Navigation Studies and Target Characterization in the Hayabusa Encounter with Itokawa," *AIAA/AAS Astrodynamics Specialist Conference and Exhibit, Keystone, Colorado*, 2006.

[7] L. Jorda, P. L. Lamy, R. W. Gaskell, M. Kaasalainen, O. Groussin, S. Besse, and G. Faury, "Asteroid (2867) Steins: Shape, topography and global physical properties from OSIRIS observations," *Icarus*, Vol. 221, No. 2, 2012, pp. 1089–1100.

[8] H. Sierks *et al.*, "On the nucleus structure and activity of comet 67P/Churyumov-Gerasimenko," *Science*, Vol. 347, No. 6220, 2015.

[9] N. Mastrodemos, B. Rush, D. Vaughan, and W. Owen, Jr., "Optical Navigation for the Dawn Mission," *23rd International Symposium on Space Flight Dynamics, Pasadena, CA, Oct 29 - Nov 2*, 2012.

[10] A. S. Konopliv, S. W. Asmar, R. S. Park, B. G. Bills, F. Centinello, A. B. Chamberlin, A. Ermakov, R. W. Gaskell, N. Rambaux, C. A. Raymond, C. T. Russell, D. E. Smith, P. Tricarico, and M. T. Zuber, "The Vesta gravity field, spin pole and rotation period, landmark positions, and ephemeris from the Dawn tracking and optical data," *Icarus*, Vol. 240, 2013, pp. 103–117.

[11] C. Wright, M. Shoemaker, J. Van Eepoel, K. DeWeese, and K. Getzendanner, "Relative Terrain Imaging Navigation Tool (Retina) for the Asteroid Robotic Redirect Mission," *39th AAS Guidance, Navigation and Control Conference, Breckenridge, CO*, 2016. AAS 16-084.

[12] R. A. Schowengerdt, *Remote Sensing (Third edition)*, ch. 8, pp. 355–385. Academic Press, 2007.

[13] J. Riedel, T. Wang, R. Werner, A. Vaughan, and D. Myers, "Configuring the Deep Impact AutoNav System for Lunar, Comet, and Mars Landing," *AIAA/AAS Astrodynamics Specialist Conference, Honolulu, HI*, 2008. AIAA 2008-6940.

[14] S. Bhaskaran, S. Nandi, S. Broschart, M. Wallace, L. Cangahuala, and C. Olson, "Small Body Landing Accuracy Using In-situ Navigation," *Advances in the Astronautical Sciences* (K. B. Miller, ed.), Vol. 141, 2011, pp. AAS 11–056.

[15] S. Bhaskaran, "Autonomous Navigation for Deep Space Missions," *AIAA SpaceOps 2012 Conference*, 2012. doi:10.2514/6.2012-1267135.

[16] Y. Cheng, D. Clouse, A. Johnson, W. Owen, and A. Vaughan, "Evaluation and Improvement of Passive Optical Terrrain Relative Navigation Algorithms for Pinpoint Landing," *Advances in the Astronautical Sciences* (M. K. Jah, Y. Guo, A. L. Bowes, and P. C. Lai, eds.), Vol. 140, 2011, pp. AAS 11–221.

[17] W. Owen, "Methods of Optical Navigation," *Advances in the Astronautical Sciences* (M. K. Jah, Y. Guo, A. L. Bowes, and P. C. Lai, eds.), Vol. 140, 2011, pp. AAS 11–215.

[18] A. McEwen, "Exogenic and Endogenic Albedo and Color Patterns on Europa," *Journal of Geophysical Research*, Vol. 81, 1986, pp. 8077–8097.

[19] A. McEwen, "A Precise Lunar Photometric Function," *Lunar and Planetary Science*, Vol. 27, 1996, pp. 841–842.

[20] R. Gaskell, "Martian Surface Simulations," *Journal of Geophysical Research*, Vol. 98, 1993, pp. 11099–11103.

[21] R. Gaskell, J. Collier, L. Husman, and R. Chen, "Synthetic environments for simulated missions," *Aerospace Conference, 2001, IEEE Proceedings.*, Vol. 7, 2001, pp. 7–3556 vol.7, 10.1109/AERO.2001.931433.

[22] C. Wright, S. Bhatt, D. Woffinden, M. Strube, and C. D'Souza, "Linear Covariance Analysis for Proximity Operations Around Asteroid 2008 EV5," *38th AAS Guidance, Navigation and Control Conference, Breckenridge, CO*, 2015. AAS 15-084.

[23] M. McKay, R. Beckman, and W. Conover, "A comparison of three methods for selecting values of input variables in the analysis of output from a computer code," *Technometrics*, Vol. 21, 1979, pp. 239–245.